Supplementary information

Free-standing graphene films decorated with lithiophilic particles as host electrode for lithium plating/stripping in anode-less lithium metal batteries

Mingliang Bai,[a] Min Zhong,*[a] Wenzhuo Shen,[a] Jiali Zhang,[a] and Shouwu Guo*[a]

a Department of Electronic Engineering, School of Electronic Information and Electrical Engineering, Shanghai Jiao Tong University, Shanghai 200240, China

* Corresponding author E-mail address:
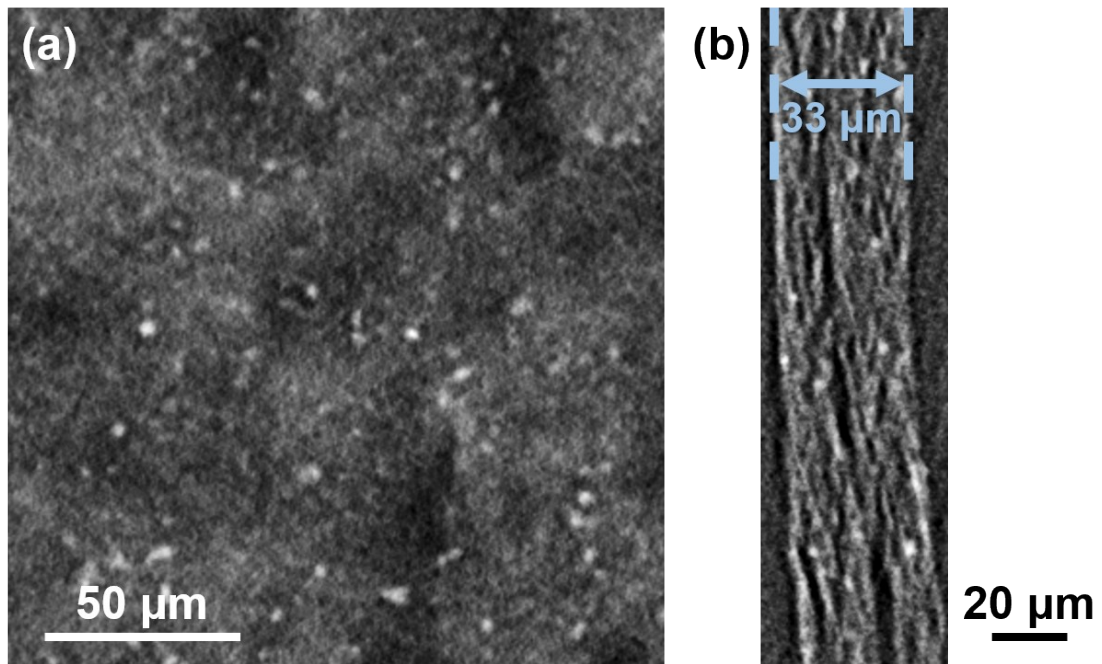Min Zhong (zomi@sjtu.edu.cn), Shouwu Guo (swguo@sjtu.edu.cn)

Fig. S1. (a) Parallel and (b) Cross-sectional XRM imaging slices of LAG film.
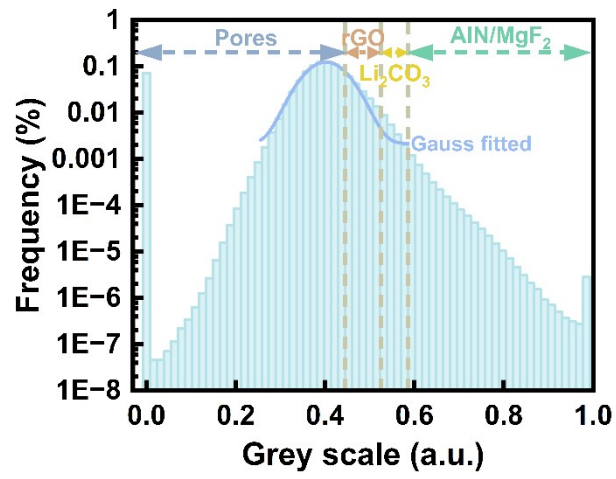
Fig. S2. Grey-scale distribution of the region corresponding to Fig. 1b.
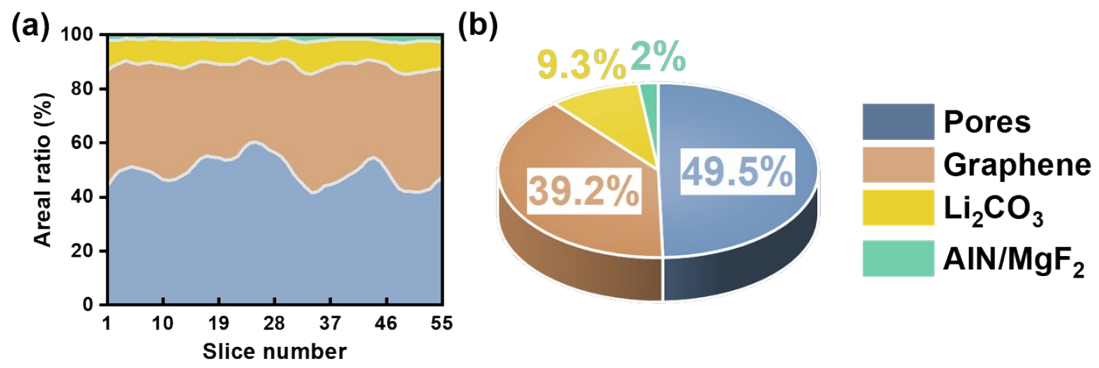
Fig. S3. (a) Areal ratios of different components in each parallel XRM slice of LAG film. (b) Average areal ratios of different components in LAG film.
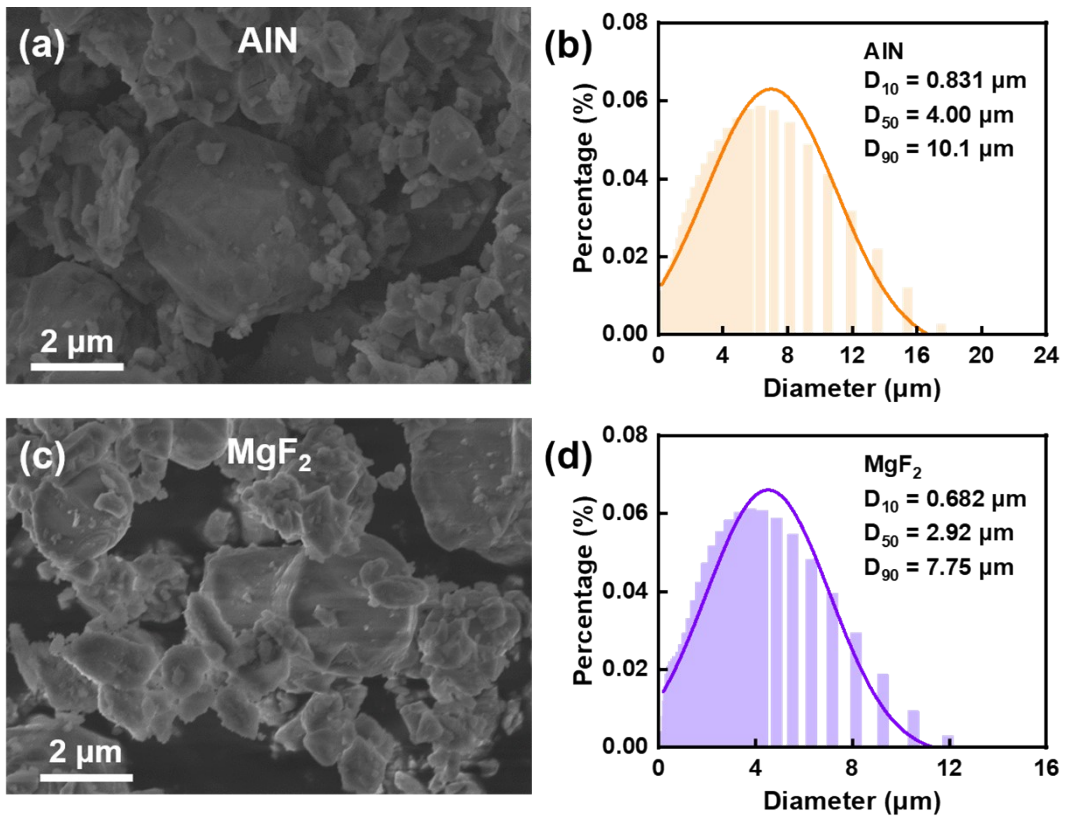
Fig. S4. SEM images and particle size distributions of originally added (a, b) AlN and (c, d) MgF$_2$ particles.
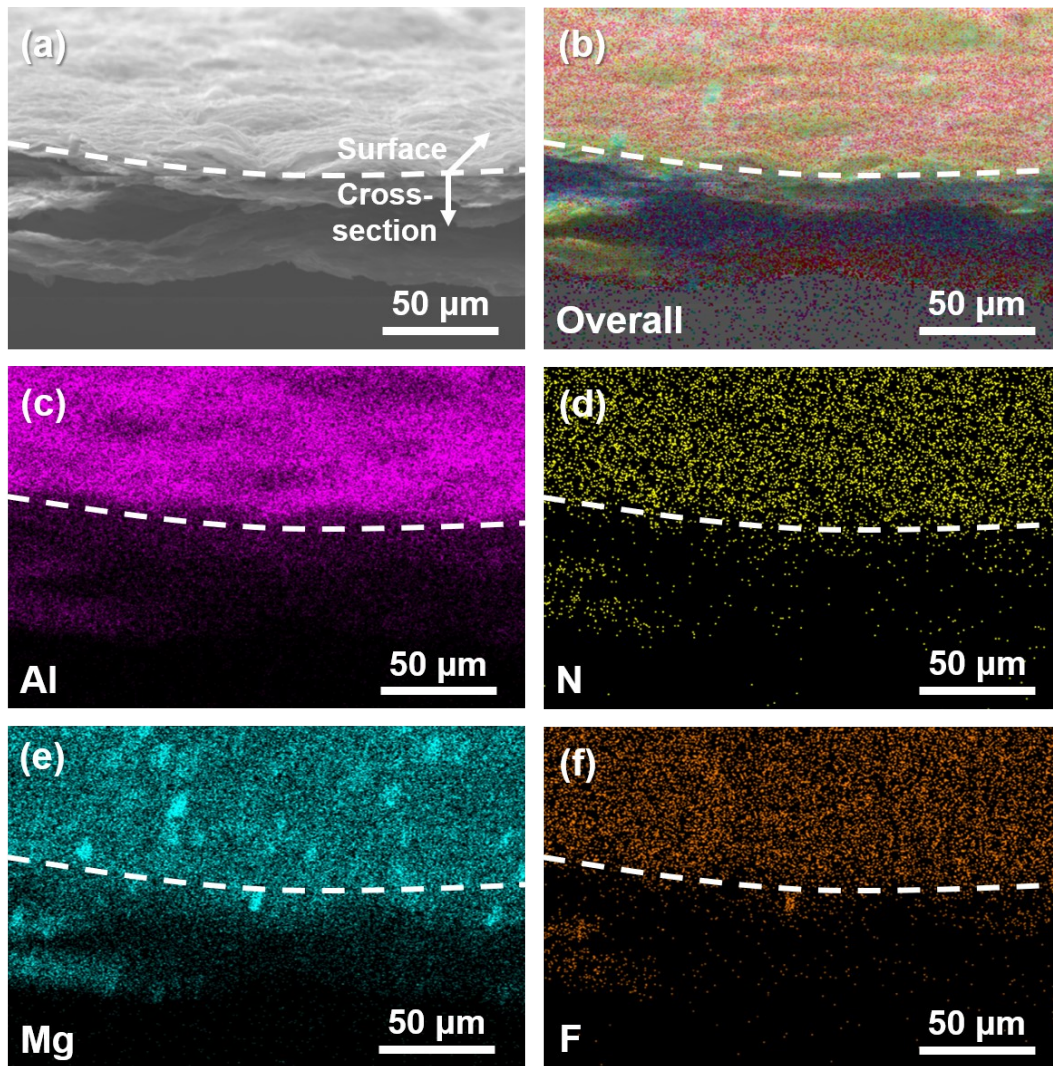
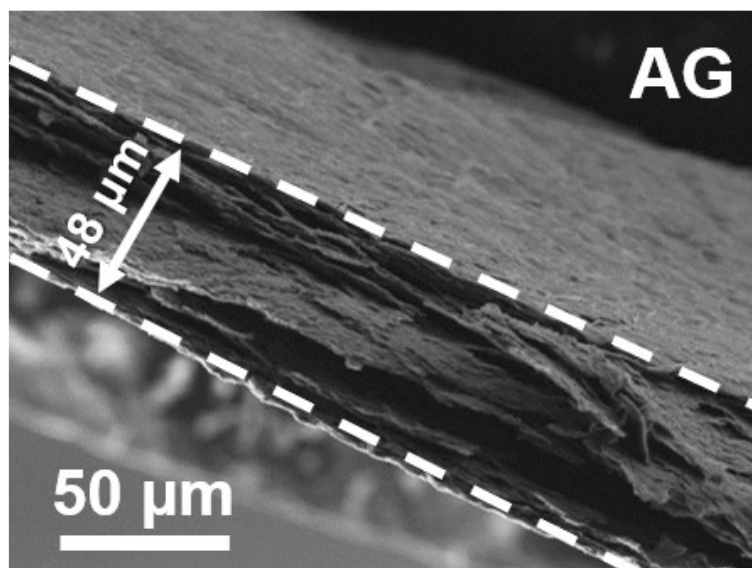Fig. S5. (a) SEM image and (b-e) EDS mapping results of LAG film.

Fig. S6. Cross-sectional SEM image of the AG film.

To build up 3D porous-scaffold structure, fast-heating method is utilized to reduce GO. A mass of H_2O molecules constrained between GO sheets rapidly vapor and burst out with CO_2, which separates graphene sheets and forms porous structure in a few seconds. Moreover, alkalization of GO precursor solution is induced, since that GO is reported to be of more thermal activity when pretreated with OH^-. According to previous studies, effects of pH on decomposition kinetics of GO are primarily due to epoxy ring opening/closing reactions upon alkalization/acidification.[1, 2] After alkalization pretreatment, the AG film maintains an integrated and relatively uniform multilayer-film structure with the thickness of ~48 μm (Fig. S6).With the addition of AlN and MgF_2, the LAG film has a more even porous structure, with the thickness of ~34 μm (Fig. 1d).
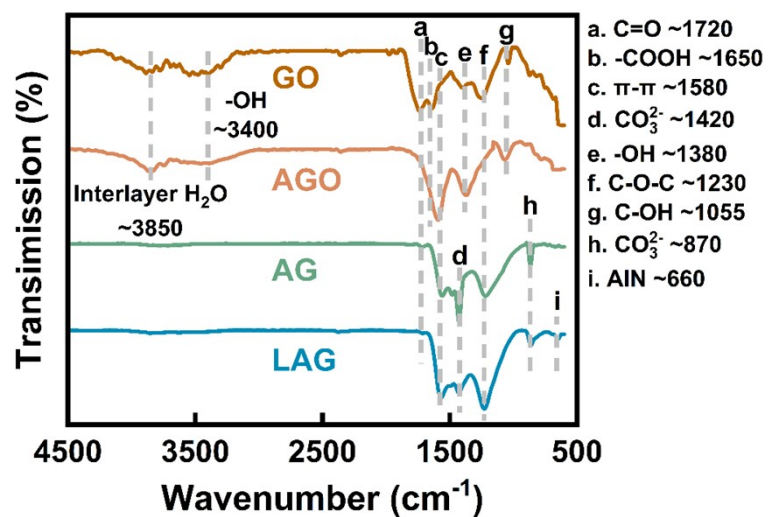
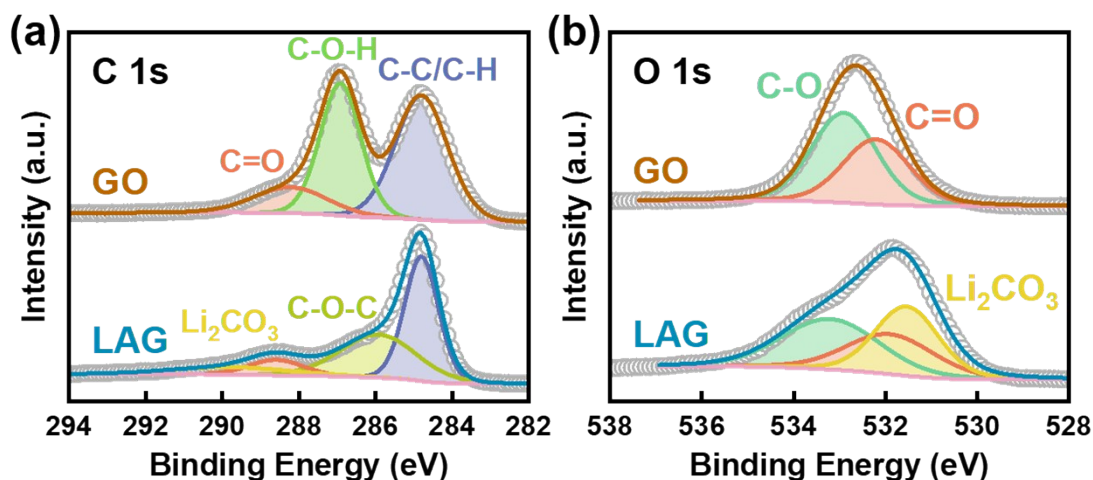Fig. S7. ATR-IR spectra of GO, AGO, AG, and LAG films.

Fig. S8. XPS spectra of (a) C 1s and (b) O 1s of GO and LAG films.

The hyperfine C 1s spectra, Fig. S8a, show the intensity of C 1s peak of C-O (C-O-H at 286.8 and C-O-C at 286.2 eV) decreasing from 43 % to 36 %, and the one of C=O (288.2 eV) descending from 14 % to 9 %. The decreasing intensities of C-O (533 eV) and C=O (532.1 eV) peaks are also obtained in O 1s spectra (Fig. S8b), from 57 % to 38 % and 43 % to 27 %, respectively. Meanwhile, C 1s and O 1s peaks appear at 289.8 and 531.5 eV correlated to Li_2CO_3 can also be observed clearly. These results imply that during the thermal reduction C=O and C-O groups may be converted into CO_2, which reacts with residual LiOH forming Li_2CO_3 and H_2O. And the as-generated H_2O is released instantly, leaving the pores within the LAG.
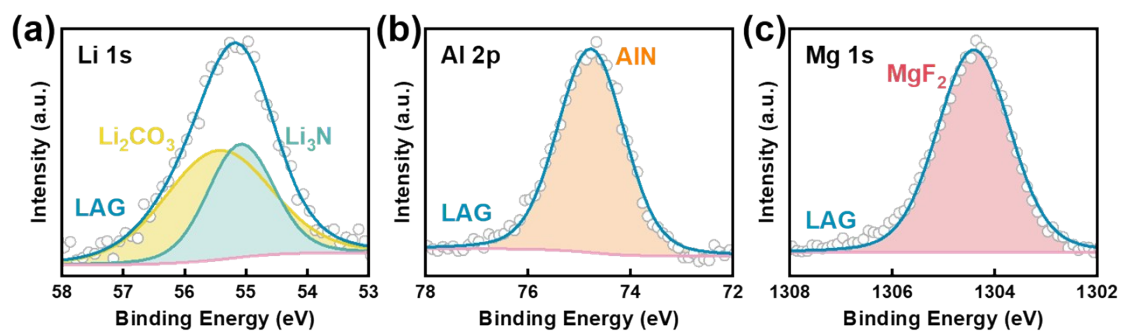
Fig. S9. XPS spectra of (a) Li 1s, (b) Al 2p and (c) Mg 1s of LAG film.
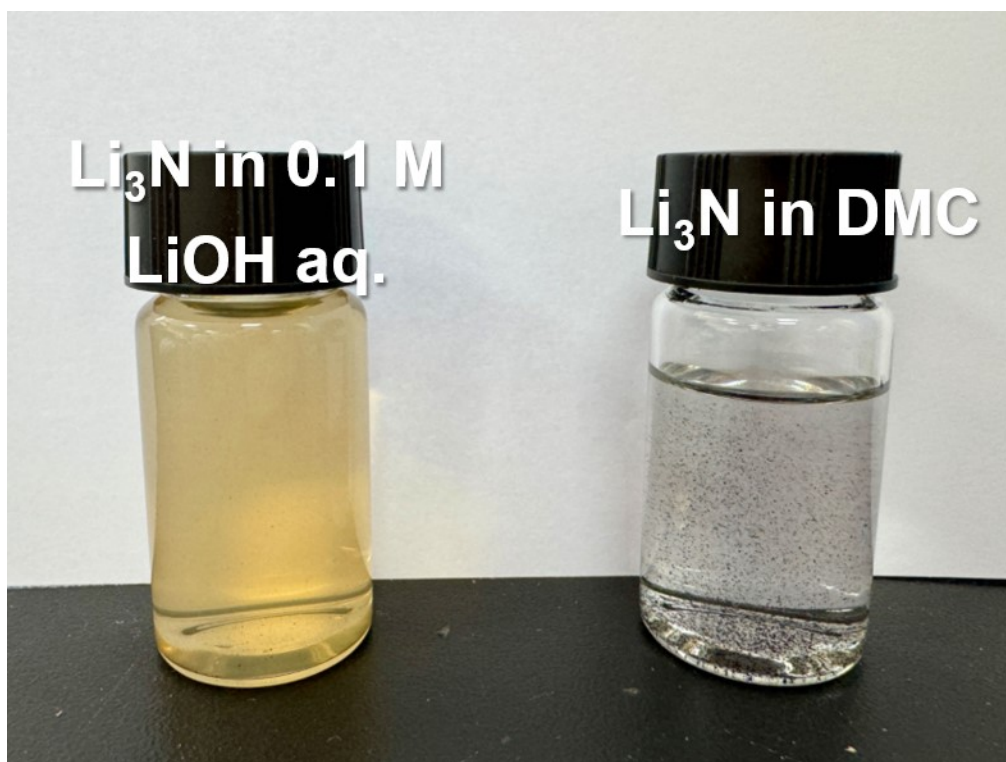
Fig. S10. Li$_3$N dispersed in 0.1 M LiOH aqueous solution and DMC for zeta potential tests.
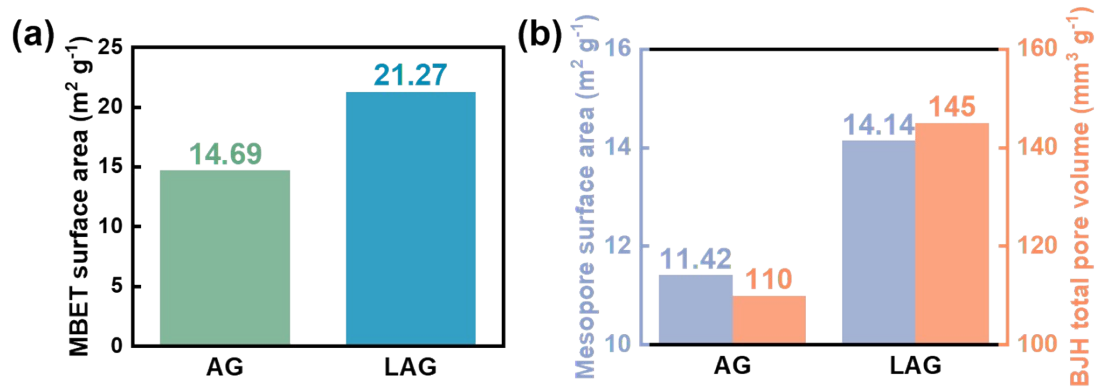
Fig. S11. (a) Multi-point BET surface areas of AG and LAG films. (b) Mesopore surface areas and BJH total pore volumes of AG and LAG films.
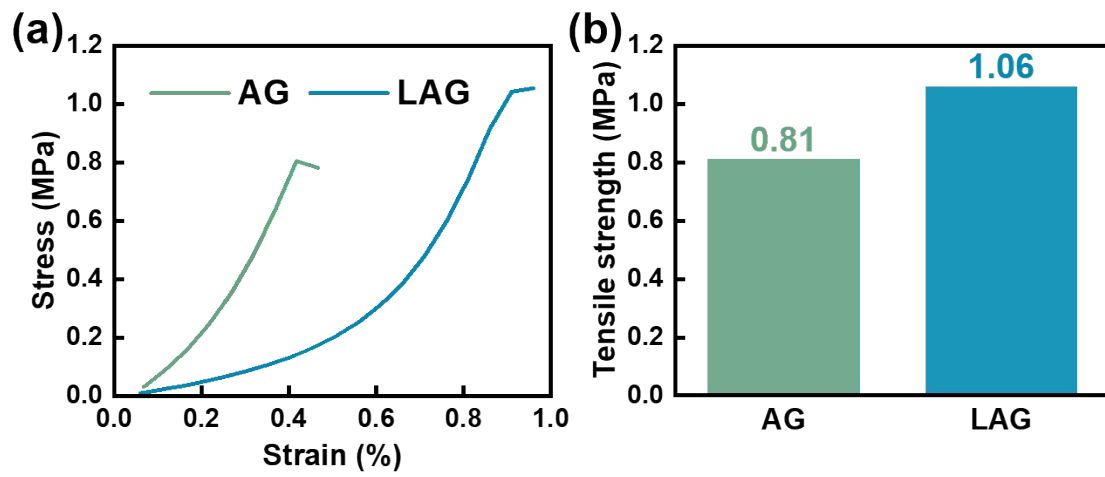
Fig. S12. (a) Stress-strain curves and (b) tensile strengths of AG and LAG films.
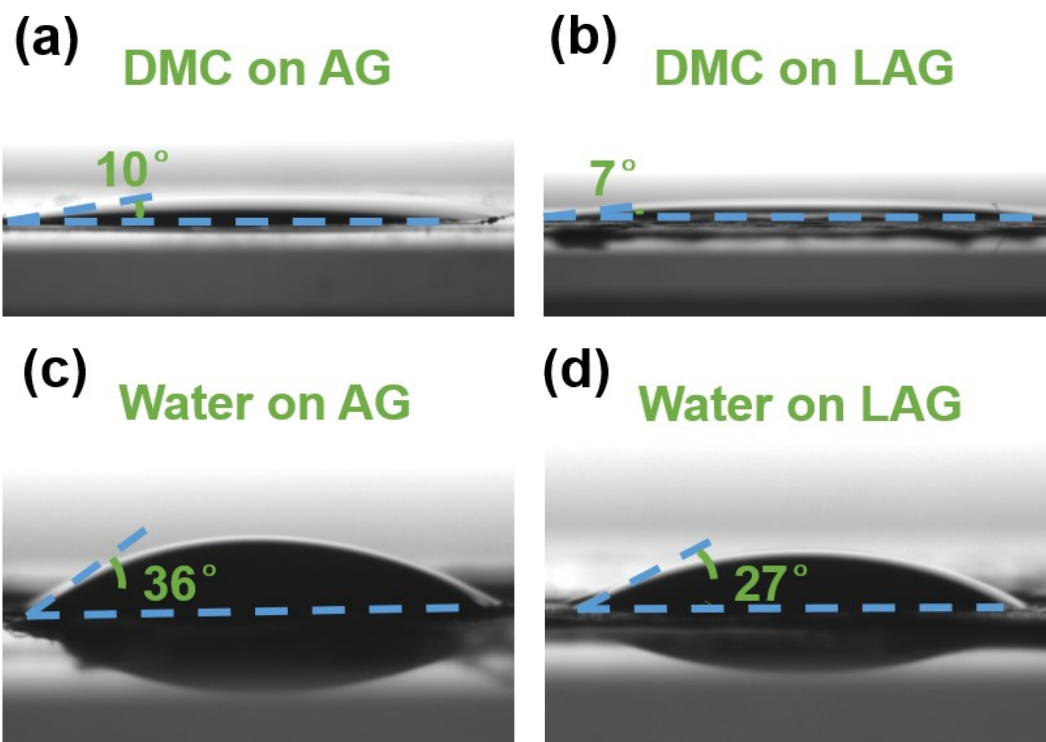
Fig. S13. Contact angles of (a, b) DMC and (c, d) water.
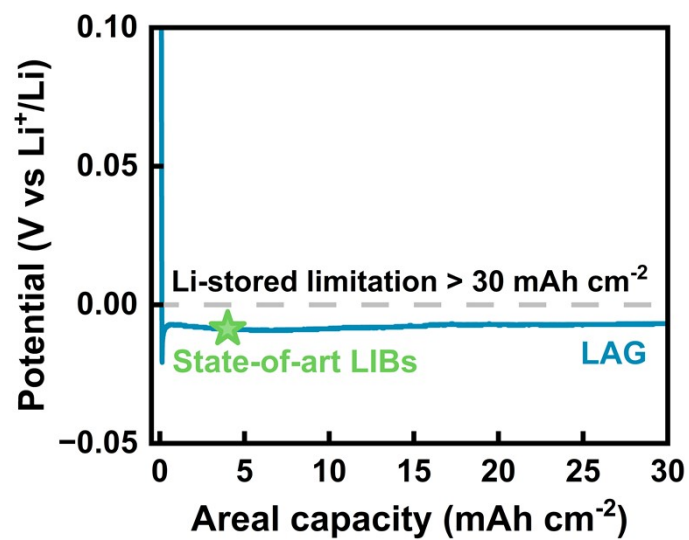
Fig. S14. Long-term lithium plating GCD curves of LAG film at 0.5 mA cm^{-2}.
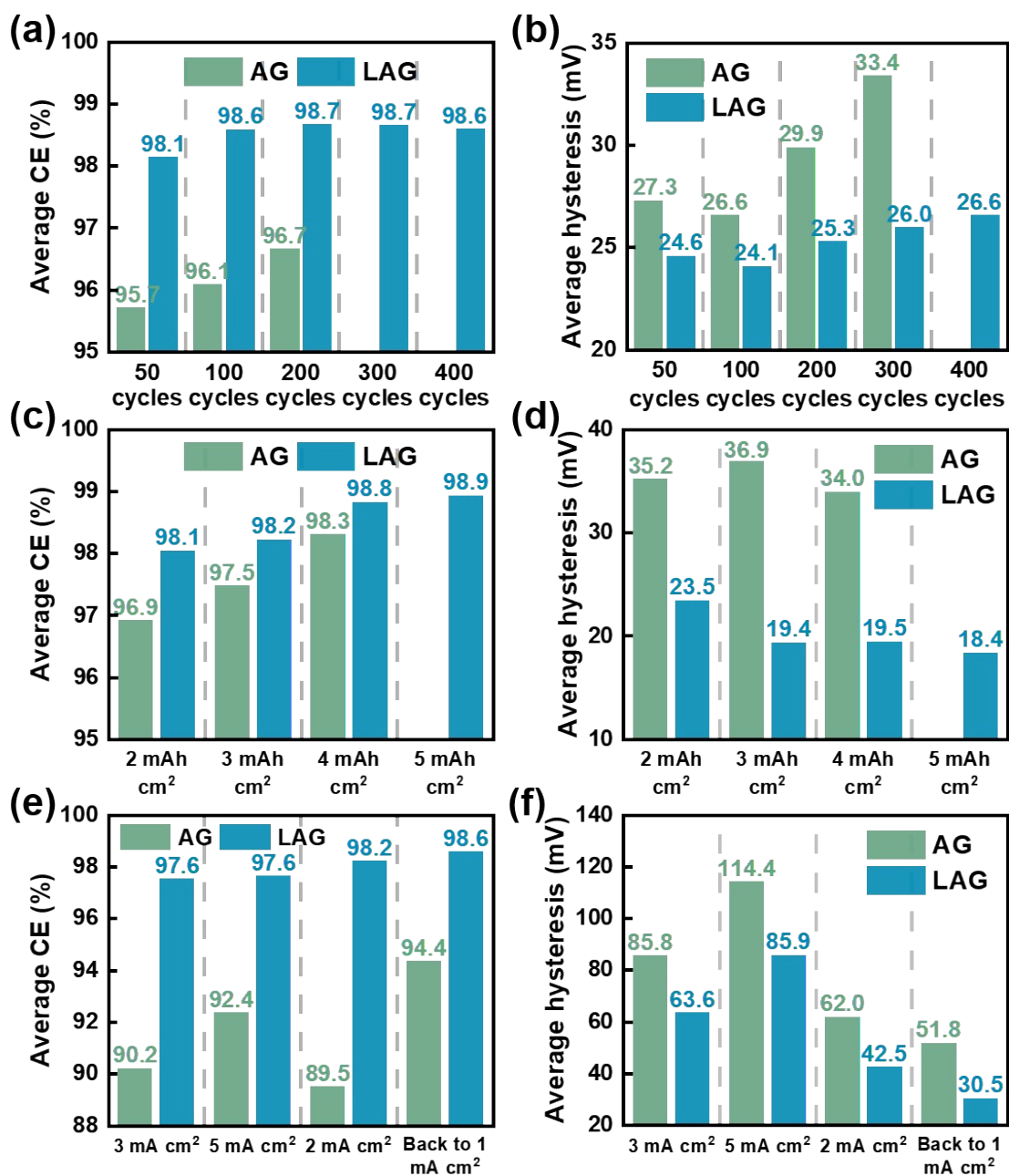
Fig. S15. (a, c, e) Average CEs and (b, d, f) average hysteresis of half-cells.
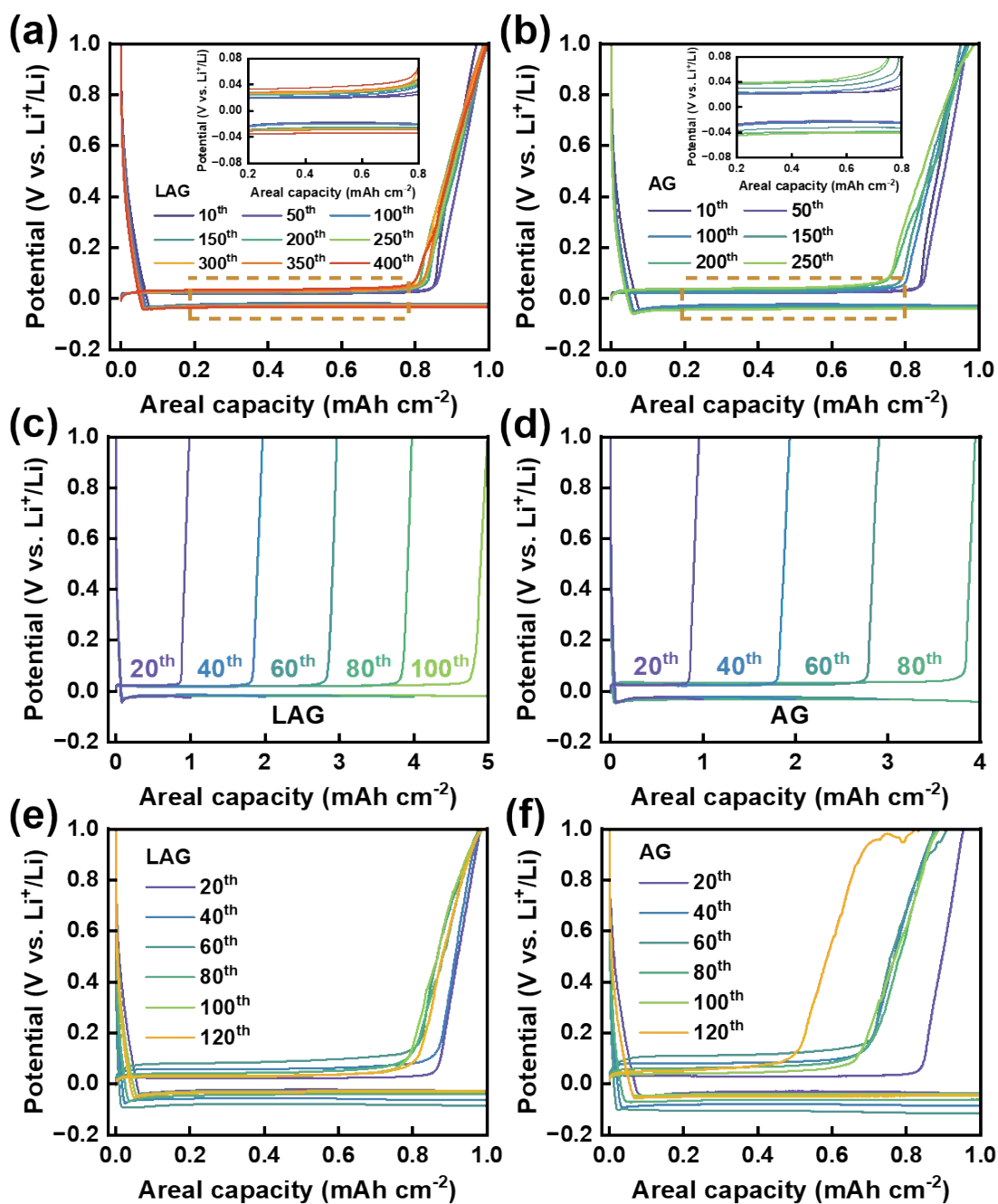
Fig. S16. GCD curves of (a) LAG and (b) AG films at 1 mA cm⁻² and 1 mAh cm⁻², (c) LAG and (d) AG films at 1 mA cm⁻² and 1 to 5 mAh cm⁻², (e) LAG and (f) AG films at 1 to 5 mA cm⁻² and 1 mAh cm⁻².
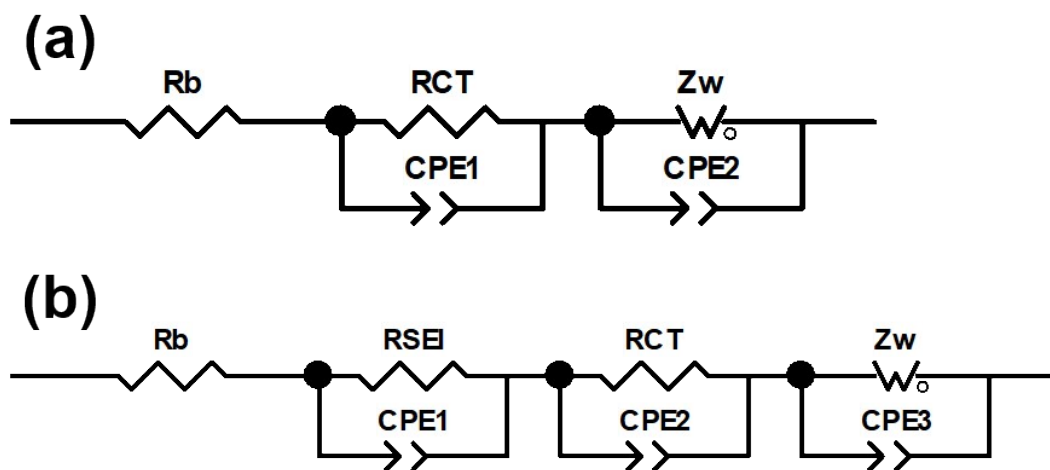
Fig. S17. The equivalent circuit of cells (a) before cycle and (b) after cycling.
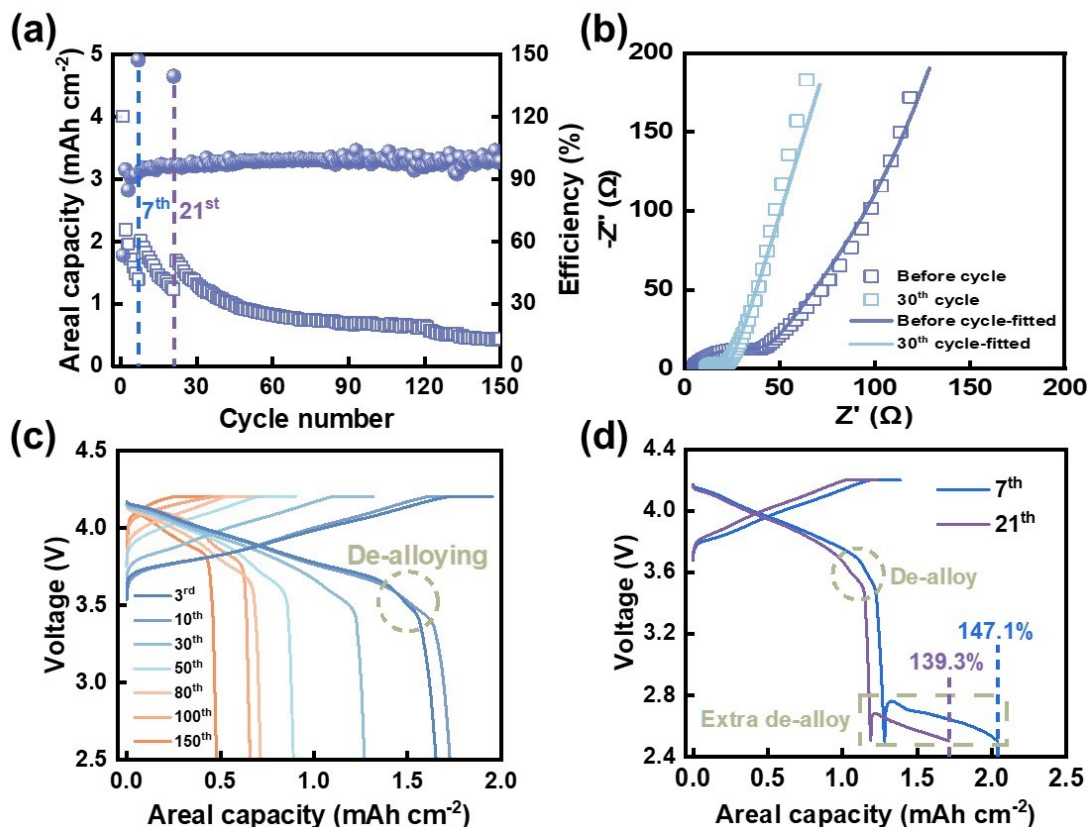
Fig. S18. (a) Cycling performance, (b) Fitted EIS curves, and GCD curves of (c) follow-up cycles, (d) 7th and 21st cycles of LA103Z‖NCM811 cell under carbonate electrolyte with FEC at 0.5C//0.5C.

Different from LAG‖NCM811 and LAG/LA103Z‖NCM811 cells, LA103Z‖NCM811 cell shows a rapid capacity decline within the initial 10 cycles, which is attributed to uncontrollable interfacial side-reaction of the alloy anodes (Fig. S18c). As the capacity decreases, LA103Z‖NCM811 cell represents aperiodic capacity recoveries at 7th and 21th cycles with CEs exceeding 130 %, which might be due to the irregular delithiation of intrinsic lithium of LA103Z foil (Fig. S18d). However, such a sudden huge capacity improvement during ZELMB cycling is not observed in LAG/LA103Z‖NCM811 cell, indicating that no irregular de-alloying occurs on LA103Z in the presence of LAG. Additionally, LA103Z‖NCM811 cell exhibits higher resistance at SOC = 0 % after 30th cycle caused by uncontrollable SEI growth on the unprotected surface (Fig. S18b, Table S3).

19
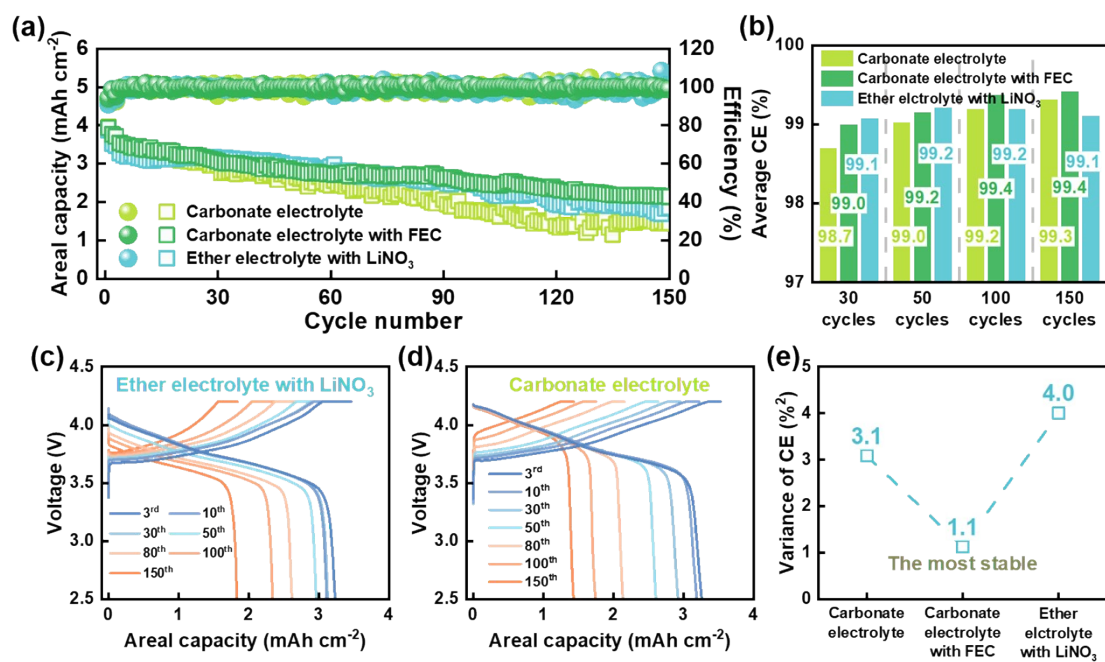
Fig. S19. Cycling performances of LAG/LA103Z‖NCM811 cells under various electrolytes at 0.5C//0.5C. (a) CEs and areal capacities. (b) Average CEs. (c-d) GCD curves. (e) Variance of CEs among 150 full-cell cycles.
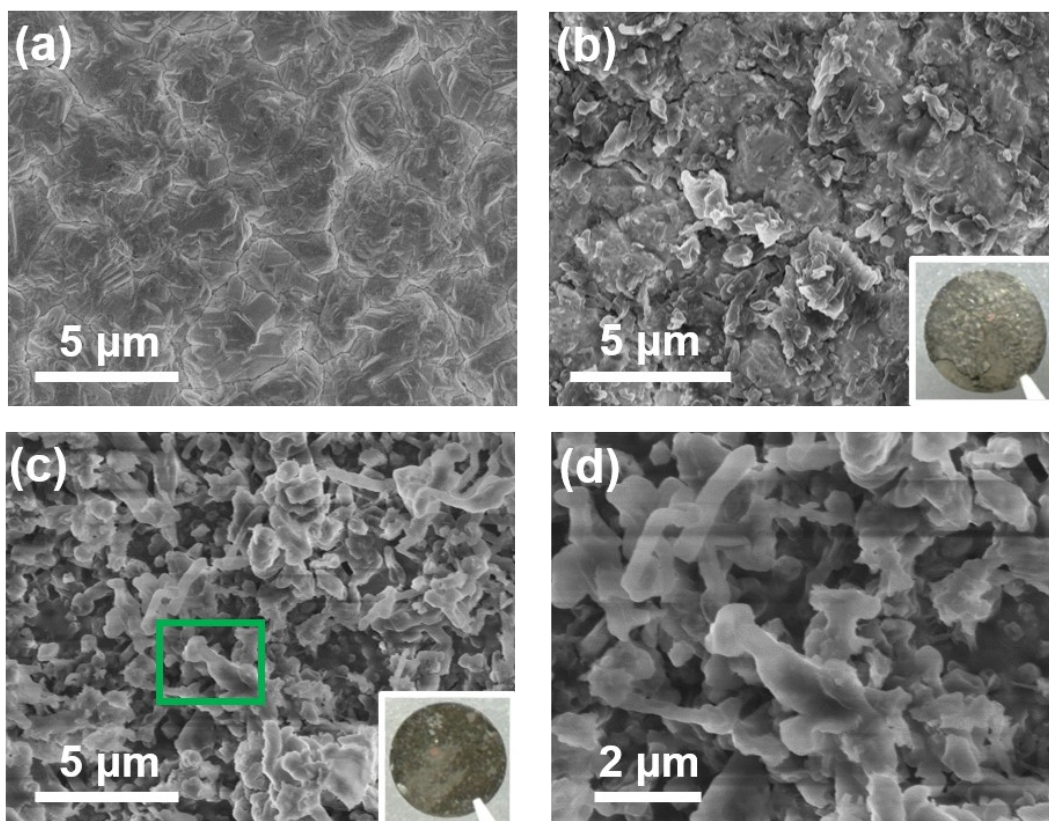
Fig. S20. SEM images of Cu foil (a) before cycle, (b) at SOC = 0 %, and (c) SOC = 100 % after 30th full-cell cycle, inset with optical images of the corresponding electrode. (d) The enlarged SEM images of green area.
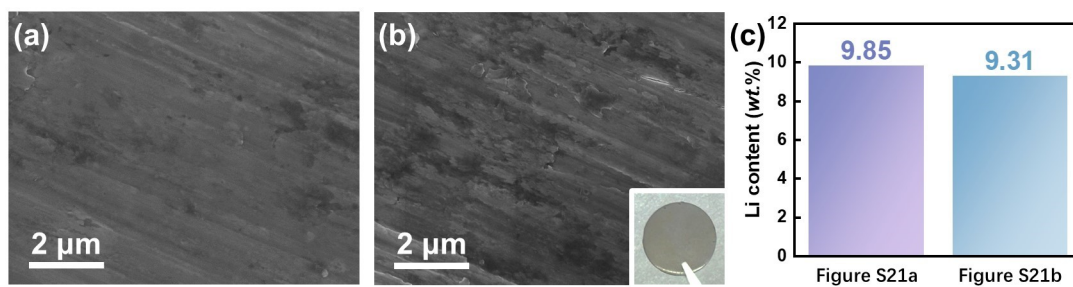
Fig. S21. SEM images of LA103Z surfaces attached to LAG (a) before cycle and (b) at SOC = 0 % after 30th full-cell cycle, inset with optical image of the corresponding surface. (c) Li contents in LA103Z correspondingly.

Fig. S21a and b compare the surficial morphologies of LA103Z foil before cycle and at SOC = 0 % after 30th full-cell cycle. Clearly, after lithium plating/stripping cycles, the surface of LA103Z is preserved as smooth as that before cycling. At the same time, the Li contents in LA103Z foil at different stages are measured using ICP-OES measurement, and the results are summarized in Fig. S21c. Notably, the Li content of LA103Z is about 9.85 *wt.* % initially, while it changes to 9.31 *wt.* % after 30 cycles, showing a slight Li loss during cycling, 0.54 *wt.* %. The slight Li loss of LA103Z after 30 cycles is attributed to continuous Li supplement, which accounts for distinguished improvement of capacity retention between LAG‖NCM811 and LAG/LA103Z‖NCM811 cells.
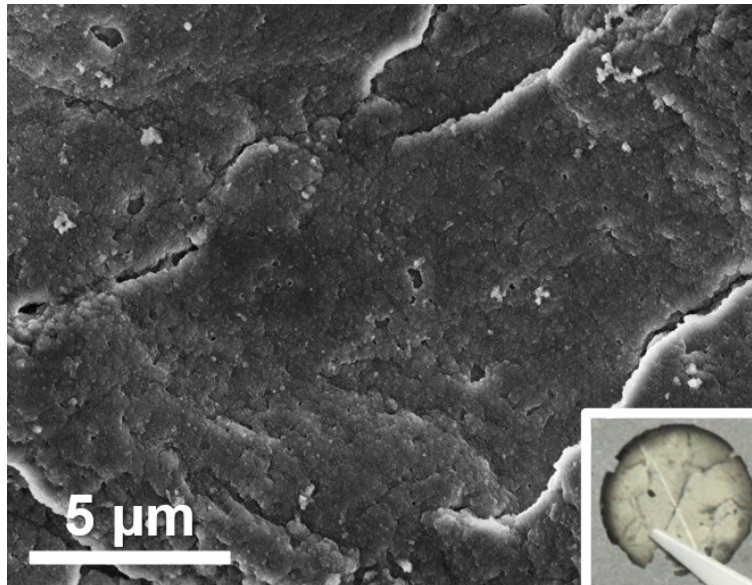
Fig. S22. SEM image of LA103Z surface at SOC = 0 % after 30th cycle of LA103Z‖NCM811 cell.
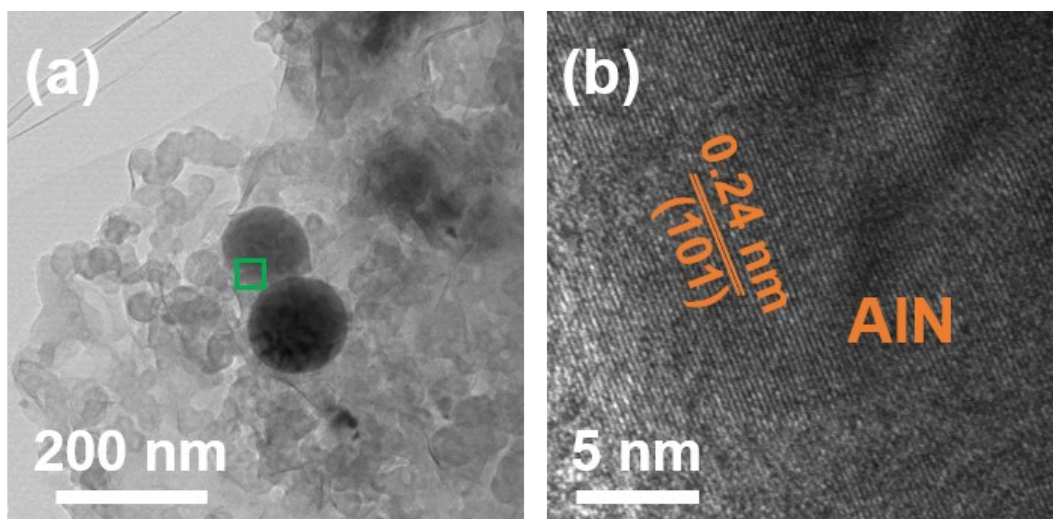
Fig. S23. TEM and HRTEM images of LAG at SOC = 0% after 30th full-cell cycle.
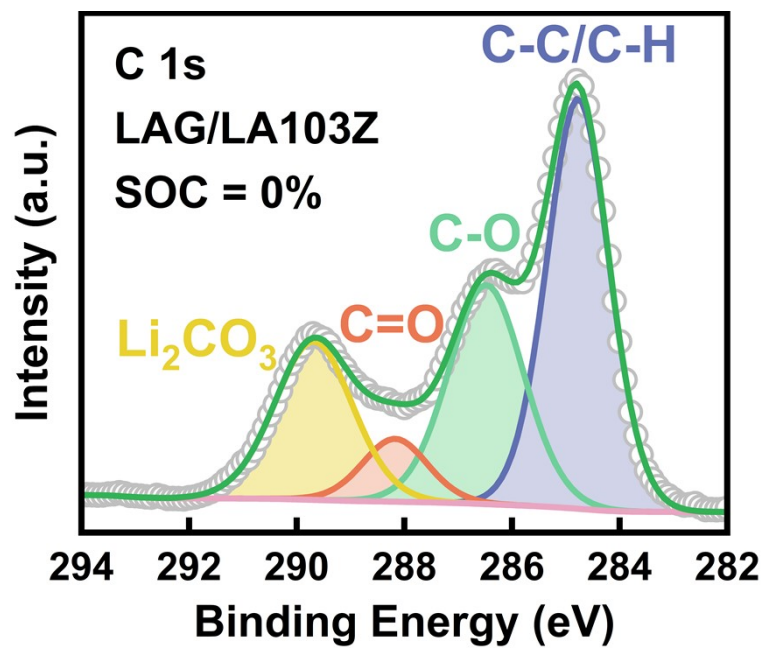
Fig. S24. Deconvoluted XPS peak of C 1s of SEI formed on LAG/LA103Z.

Table S1. Atomic percentage of chemical states calculated by deconvoluted XPS spectra of LAG and GO.

Samples	Spectra	Chemical states	Atomic percentage
GO	C 1s	C-C/C-H	43.6%
		C-O-H	42.6%
		C=O	13.8%
	O 1s	C=O	42.9
		C-O	57.1
LAG	C 1s	C-C/C-H	45.5%
		C-O-C	35.5%
		C=O	9.1%
		Li_2CO_3	9.9%
	O 1s	Li_2CO_3	34.4%
		C=O	27.3%
		C-O	38.3%
	N 1s	AlN	71.1%
		Li_3N	28.9%
	F 1s	MgF_2	100%
	Li 1s	Li_3N	39.2%
		Li_2CO_3	60.8%
	Al 2p	AlN	100%
	Mg 1s	MgF_2	100%

Table S2. Fitted EIS results of half-cells.

Electrode		R_b (Ω)	R_{SEI} (Ω)	R_{CT} (Ω)	χ^2
Before cycle	Cu	2.24	/	120	0.069
	AG	2.38	/	77.4	0.030
	LAG	3.81	/	65.9	0.005
50th cycle SOC = 0%	Cu	21.7	157	226	0.052
	AG	9.87	18.4	59.8	0.024
	LAG	7.02	10.0	5.05	0.031

Table S3. Physical parameters of the LA103Z foil.

	LA103Z foil			
Element contents (*wt.* %)	Li	Mg	Al	Zn
	~10	~84	~3	~3
Thickness (μm)	50			
Density (g cm^{-3})	1.45			
Areal density (mg cm^{-2})	7.25			

Table S4. Fitted EIS results of full-cells.

Electrode		R_b (Ω)	R_{SEI} (Ω)	R_{CT} (Ω)	χ^2
Before cycle	LAG	22.0	34.3	22.9	0.003
	LA103Z	4.19	41.2	80.5	0.039
	LAG/LA103Z	4.04	10.5	13.1	0.006
30th cycle SOC = 0%	LAG	14.5	12.0	13.4	0.002
	LA103Z	10.9	10.0	43.2	0.053
	LAG/LA103Z	2.96	7.84	10.9	0.007

Table S5. Comparison of electrochemical performance of anode-free cells reported in previous works, corresponding to Fig. 4g.

Design type	Areal capacity (mAh cm^{-2})	Charge current density (mA cm^{-2})	Discharge current density (mA cm^{-2})	Electrolyte	Cycles	Capacity retention	Reference
Host	3.86	1.93		1 M LiPF$_6$ in EC/DEC/DMC (1/1/1, in *vol.*) with 10 *vol.* % FEC	50	71.4 %	This work
					100	63.7 %	
					120	60.0 %	
Host	4.2	2.1		1.3 M LiPF$_6$ in EC/DEC (3/7, in *vol.*) with 10 % FEC	100	52 %	Ref 3
Electrolyte	~3.1	0.62	1.55	High-entropy fluorinated diethoxyethane-based F3-6DEE	70	~48 %	Ref 4
				High-entropy carbonate-based EL5c	50	~60 %	
Host	~1.7	0.34		5 M LiFSI and 0.1 M LiPF$_6$ in FEC/DMC/TTE (1/2/2, in *vol.*)	100	50 %	Ref 5
Host	1.8	0.9		4 M LiFSI in DME	100	~46 %	Ref 6
Electrolyte	2.4	0.48	1.2	1 M LiBF$_4$ in FEC/DEC (1/2, in *vol.*)	50	~15 %	Ref 7
				0.6 M LiDFOB and 0.6 M LiBF4 in FEC/DEC (1/2, in *vol.*)	100	~52 %	
				1 M LiDFOB and 0.2 M LiBF$_4$ in FEC/DEC (1/2, in *vol.*)	100	~72 %	
Electrolyte	2.04	0.204	1.02	Carbonate-based LPFN-i2	80	~29 %	Ref 8
Host	~2.25	0.5		1 M LiPF$_6$ in EC/DEC (1/1, in *vol.*) with 5 % FEC	60	~56 %	Ref 9

Design type	Areal capacity (mAh cm-2)	Charge current density (mA cm-2)	Discharge current density (mA cm-2)	Electrolyte	Cycles	Capacity retention	Reference
Electrolyte	~0.48	~0.144		0.15M $LiNO_3$ and 0.1 M $LiPF_6$ in SL/FB (1/1, in *vol.*) with 5 *wt.* % FEC	50	~57 %	Ref 10
Electrolyte	2	0.2	1	Carbonate-based C-LDH-BE-LN	40	~35%	Ref 11
Host	1	0.2		1 M LiDFOB + 0.2 M $LiBF_4$ in FEC/DEC (1/2, in *vol.*)	50	~47%	Ref 12
Host	1.6	0.8		1 M LiFSI in DME	40	~22%	Ref 13
Interlayer	~0.8	~0.4		1 M LiTFSI in DME/DOL (1/1, in *vol.*) with 3 *wt.* % $LiNO_3$	80	~43%	Ref 14
		~0.8			40	~28%	

Table S6. Atomic percentage of chemical states calculated by deconvoluted XPS spectra of SEI formed on LAG/LA103Z.

Spectra	Chemical states	Atomic percentage
C 1s	C-C/C-H	43.7%
	C-O-H	25.1%
	C=O	5.8%
	Li_2CO_3	25.4%
O 1s	Li_2CO_3	51.3%
	C=O	36.0%
	C-O	12.7%
N 1s	Li_3N	82.3%
	Li_xNO_y	17.7%
F 1s	LiF	61.4%
	$Li_xPO_yF_z$	31.5%
	Li_xPF_y	7.1%
Li 1s	$ROCO_2$-Li	4.5%
	Li_2CO_3	26.4%
	Li_3N	18.8%
	LiF	50.3%

References

1. Y. Zhu, S. Murali, M. D. Stoller, K. J. Ganesh, W. Cai, P. J. Ferreira, A. Pirkle, R. M. Wallace, K. A. Cychosz, M. Thommes, D. Su, E. A. Stach and R. S. Ruoff, *Science*, 2011, **332**, 1537-1541.
2. Z. Tan, K. Ni, G. Chen, W. Zeng, Z. Tao, M. Ikram, Q. Zhang, H. Wang, L. Sun, X. Zhu, X. Wu, H. Ji, R. S. Ruoff and Y. Zhu, *Adv. Mater.*, 2017, **29**, 1603414.
3. S. Cho, D. Y. Kim, J.-I. Lee, J. Kang, H. Lee, G. Kim, D.-H. Seo and S. Park, *Adv. Funct. Mater.*, 2022, **32**, 2208629.
4. S. C. Kim, J. Wang, R. Xu, P. Zhang, Y. Chen, Z. Huang, Y. Yang, Z. Yu, S. T. Oyakhire, W. Zhang, L. C. Greenburg, M. S. Kim, D. T. Boyle, P. Sayavong, Y. Ye, J. Qin, Z. Bao and Y. Cui, *Nat. Energy*, 2023, **8**, 814-826.
5. X. Liao, X. Wang, C. Yan, B. Zhang, Y. Ni, H. Yuan, Y. Pan, J. a. Pan and J. Huang, *Adv. Funct. Mater.*, 2024, DOI: 10.1002/adfm.202310925, 2310925.
6. W. Chen, R. V. Salvatierra, M. Ren, J. Chen, M. G. Stanford and J. M. Tour, *Adv. Mater.*, 2020, **32**, 2002850.
7. R. Weber, M. Genovese, A. J. Louli, S. Hames, C. Martin, I. G. Hill and J. R. Dahn, *Nat. Energy*, 2019, **4**, 683-689.
8. Z. Wen, W. Fang, X. Wu, Z. Qin, H. Kang, L. Chen, N. Zhang, X. Liu and G. Chen, *Adv. Funct. Mater.*, 2022, **32**, 2204768.
9. Z. T. Wondimkun, W. A. Tegegne, J. Shi-Kai, C.-J. Huang, N. A. Sahalie, M. A. Weret, J.-Y. Hsu, P.-L. Hsieh, Y.-S. Huang, S.-H. Wu, W.-N. Su and B. J. Hwang, *Energy Storage Mater.*, 2021, **35**, 334-344.
10. P. Li, H. Zhang, J. Lu and G. Li, *Angew. Chem. Int. Ed.*, 2023, **62**, e202216312.
11. F. Wang, Z. Wen, Z. Zheng, W. Fang, L. Chen, F. Chen, N. Zhang, X. Liu, R. Ma and G. Chen, *Adv. Energy Mater.*, 2023, **13**, 2203830.
12. T. T. K. Ingber, M. M. Bela, F. Püttmann, J. F. Dohmann, P. Bieker, M. Börner, M. Winter and M. C. Stan, *J. Mater. Chem. A*, 2023, **11**, 17828-17840.
13. J. Jung, J. Y. Kim, I. J. Kim, H. Kwon, G. Kim, G. Doo, W. Jo, H.-T. Jung and H.-T. Kim, *J. Mater. Chem. A*, 2022, **10**, 20984-20992.
14. O. Tamwattana, H. Park, J. Kim, I. Hwang, G. Yoon, T.-h. Hwang, Y.-S. Kang, J. Park, N. Meethong and K. Kang, *ACS Energy Lett.*, 2021, **6**, 4416-4425.